Constructive versus Destructive Heterogeneity in Porous Electrodes of Lithium-Ion Batteries

YARI, Saeed; HAMED, Hamid; D'HAEN, Jan; VAN BAEL, Marlies; RENNER, Frank; HARDY, An & SAFARI, Momo (2020) Constructive versus Destructive Heterogeneity in Porous Electrodes of Lithium-Ion Batteries. In: Acs Applied Energy Materials, 3 (12) , p. 11820 -11829.

DOI: 10.1021/acsaem.0c01966
Handle: http://hdl.handle.net/1942/33850

Constructive Versus Destructive Heterogeneity in the Porous Electrodes of Lithium-Ion Batteries

Saeed Yari, [1-2] Hamid Hamed, [1-2] Jan D'Haen,[1,3] Marlies K. Van Bael,[1-3] Frank Uwe Renner, [1-3] An Hardy, [1-3] Mohammadhosein Safari[1-3,*]

[1]*Institute for Materials Research (IMO-imomec), UHasselt, Martelarenlaan 42, B-3500 Hasselt, Belgium*

[2]*Energyville, Thor Park 8320, B-3600 Genk, Belgium*

[3]*IMEC division IMOMEC, BE-3590, Belgium*

ABSTRACT

We introduce an efficient framework for investigating the heterogeneity in the battery porous electrodes and its impacts on the performance and longevity of the lithium-ion batteries. A phenomenological picture based on theory and experiment is presented to show how the spatial variations in the local porosity and thickness in a porous electrode result from a microscopically inhomogeneous slurry. A series of analogous bilayer $LiNi_{0.6}Mn_{0.2}Co_{0.2}O_2$ porous electrodes with different levels of heterogeneity, induced by a non-uniform distribution of carbon, is prepared as a model experimental system and established as a powerful tool in formalizing the concept of heterogeneity. We identify and distinguish between the constructive and destructive heterogeneity as the two shades of non-uniformity in the porous electrodes. Depending on the degree of heterogeneity, we observe up to 20% decline in the rate performance of the electrodes. The destructive and constructive heterogeneity in the analogous electrodes are manifested in 5 fold increase and 2 fold decrease, respectively, in the aging rate of $Li_4Ti_5O_{12}|LiNi_{0.6}Mn_{0.2}Co_{0.2}O_2$ cells relative to that of a cell with a homogenous electrode after 200 cycles at 1C.

KEYWORDS

Li-ion battery, NMC cathode, inhomogeneity, aging, bilayer electrode

1. INTRODUCTION

Li-ion batteries revolutionized the energy storage technology, but still attract much attention from the battery research community to improve their energy, power, cycle life, and safety.[1,2] This is being addressed mainly by research on the novel electrode materials,[3–5] electrode architectures and cell design.[6–8] The aim of this study is to

investigate the sensitivity of the battery electrode performance and longevity to the state of electrode characteristics by putting the emphasize on the homogeneity for this is very crucial but least studied in the literature.

Inhomogeneity in a battery electrode might be defined as a non-zero directional gradient in the physical and/or chemical properties of the porous coat on top of the current collector. In Li-ion battery electrodes, such inhomogeneity is caused by an uneven distribution of the active material, carbon, binder and electrolyte. [9–16] Such heterogeneities can affect the active material utilization and transport properties and hence impact the energy density, power performance, and ageing dynamics of the cell both in-plane and through-plane of the electrode. [17–21] The electrode design and/or the processing steps can inadvertently introduce heterogeneities in a porous electrode. An inexpert mixing or electrode slurry formulation could induce phase segregation, particle flocculation, composition gradients owing to settlement of heavy active materials, and causes localization of active material or creates a poor electronic percolation in the carbon matrix. [22–27] The important role of carbon distribution in the electrode performance has been spotlighted by using different slurry mixing procedures. [22,23] Inhomogeneity in the binder distribution becomes more prominent during the drying step, where migration of binder to the upper most layers of the electrode could occur due to capillary forces. [14,28,29] The migration of binder and its accumulation at the electrode surface diminishes the ion transport in the electrolyte by increasing the electrode tortuosity near the separator. There is a concurrent reduction in the electronic conductivity of the electrode near the current collector due to the depletion of carbon-binder domains at electrode-current collector interface. [14,30,31] Ultra-thick electrode design, is a new approach to enhance the energy density while reducing the battery production costs. [6,32,33] Thick electrodes, however, suffer from a sluggish rate performance ascribed to the poor effective transport properties in solid and liquid phases due to the formation of pinhole defects together with the migration, settlement, and segregation of electrode components during coating and drying steps. [32–34]

In this work, a theoretical and experimental framework is presented to facilitate formalizing the concept of heterogeneity in the porous electrodes of lithium-ion batteries and its consequences on the battery performance. We realized our investigation with $LiNi_{0.6}Mn_{0.2}Co_{0.2}O_2$ that is a cathode active material (NMC622). NMCs are state-of-the-art family of cathodes that have the potential to increase the energy density of Li-ion batteries, while being susceptible to the cathode electrolyte interphase (CEI) formation and surface crystal reconstruction upon

cycling. [35–38] We start by developing a simple design framework for the formulation and preparation of the porous electrodes with two direct implications in this paper. First, to identify the most crucial state identifiers of the NMC electrode slurry and to draw a physical picture to juxtapose the non-uniformity of the slurry and the microstructural heterogeneity of the electrode. Second, to enable the preparation of reproducible bilayer NMC porous electrodes with a desired level of contrast in the carbon content between the two layers. The bilayer electrodes are employed to build an experimental model system consisting of six analogous NMC electrodes with the same total loading of carbon but different spatial distribution. The electrodes at different levels of heterogeneity are evaluated in Li|NMC and $Li_4Ti_5O_{12}$|NMC cells for their electrochemical performance and aging rate in a series of complementary characterizations, i.e. electrochemical (dis)charge, electrochemical impedance spectroscopy, restricted diffusion, sheet resistance, surface roughness, and SEM.

2. EXPERIMENTAL SECTION

2.1. Materials and Electrode Fabrication

In this work electrode slurries were made by mixing NMC622 (commercial product) as active materials, with carbon black (Super-C45, Imerys), and PVDF binder (Solef 5130, Solvay) that was dissolved in NMP solvent (Carl Roth). For the mixing purpose, the carbon was first added to the solution of binder in NMP and mixed under vacuum in Thinky centrifugal mixer. Later, the active material was added to the dispersion and mixed for an additional 10 minutes. Final porous electrodes were made by applying the slurries on Al foil with doctor blade coating and subsequent drying in the oven at 110 °C.

Three series of electrodes were fabricated. In the first series the carbon content was adjusted at 1, 2.5 and 4 wt.% and the coating blade gap was at a fixed value of 235 microns; these electrodes were fabricated for characterization purpose where electrode porosity, loading, surface roughness and morphology was investigated. In the second series single layer electrodes were made with total carbon content of 1, 1.5, 2, 2.5 , 3, 3.5 and 4 wt.% and the coating blade gap was adjusted to result in ~ 11 mg/cm^2 of active material in the dried coat. In the third series bilayer electrodes were made with total carbon content of 2.5 wt.% and total active material loading of ~11 mg/cm^2. Bilayer electrodes were fabricated by a coating/semi-drying/coating technique where the first coat was slightly dried before applying the second coat. Further details on bilayer electrode fabrication is presented in supplementary

information and Fig. S1. The two last series of electrodes were used to investigate the electrochemical performance in coin cells and were calendared to 30% porosity in advance. In all electrode slurries the percentage of active material and PVDF binder were adjusted to result in a constant thickness of binder covering the total available surface of carbon and active material [39] using eqn. S1. The complete AM:C:B formulation and the physical properties of each components (S_i, ρ_i) are presented in Table S1.

2.2. Characterizations of Slurry and Porous Electrodes

A series of characterization methods including rheometery, surface and cross section SEM and surface roughness analysis as well as porous electrode electronic conductivity, i.e. sheet resistance, and ionic conductivity, i.e. tortuosity, were conducted. In brief, the slurry viscosity was measured by an MCR 302 rheometer from Anton Paar with a parallel plate measuring system at shear rate of 1 to 500 1/s. Cross section of NMC electrodes were characterized by embedding them in epoxy resin followed by cutting, grinding with SiC paper and subsequent polishing with diamond suspension. 6 nm carbon coat was sputtered on the prepared sample for better conductivity. An FEI Quanta 200FEG SEM was used for imaging at 15kV. The surface roughness of the electrodes was assessed with a 3D laser scanning confocal microscope at 50X (Keyence). The electronic conductivity of the electrode coats on a nonconductive, chemically resistant substrate (Kapton film, Dupont) was measured using a four-point probe setup (Ossila) at room temperature. The tortuosity of the single layer electrodes was determined in Li-Li symmetric cell following the restricted-diffusion method developed by Thorat et al. [40] Further details about the characterization experiment can be found in the supplementary information.

2.3. Electrochemical Measurements

Standard 2025 coin cells were fabricated for the electrochemical tests. First, electrode punches were dried overnight at 110 °C in a vacuum oven to remove any residual moisture, and then were transferred into an Ar-filled M-Braun glovebox with oxygen and water content of less than 1 pmm. Half cells were assembled in front of Li foil using Celgard 2325 as separator and EC:EMC 3:7, 1M $LiPF_6$ + 2wt.% VC as electrolyte. After assembly, the cells were allowed to rest for 24 hours and then were formed by two consecutive charge and discharge cycles at C/10, in the potential window of 3.0-4.3 V, using a BCS-805 battery cycler from Biologic. Rate capability test was performed by applying a constant current (CC) (dis)charge at 0.5C, 1C, 2C and 3C followed by a constant

voltage step (CV) until the current dropped below C/20. The CV step used to ensure the full (de)lithiation of the electrodes. The cells were left to rest for 15 minutes after each CC-CV discharge step. A C/10 rate corresponds to 0.175 mA per milligram of active material.

Galvanostatic aging cycling of Li|NMC cells was performed for 50 cycles at C/3 charge and C/2 discharge rate. Before cycling, while in the full discharge state, the EIS response was recorded in the frequency range of 10kHz-100mHz with a voltage amplitude of 5 mV. When cycling ended, the cells were disassembled and cathode punches were rinsed with DMC solvent for 30 seconds to remove electrolyte salt and possible degradation products and were allowed to dry overnight. New coin cells with the recovered aged cathodes were assembled using fresh electrolyte, separator and Li foil. These cells after 24 hours of rest were subject to the formation cycles, residual capacity measurement at C/10, and EIS measurement. Full cells of NMC/LTO were prepared by using commercial LTO foil (Customcells, Germany) with identical separator and electrolyte as of half cells. After 3 formation cycles at C/10, the cells were galvanostatically (dis)charged at 1C for 200 cycles in a potential range of 1.4 and 2.8 V. The evolution in the residual capacity of the cells was recorded with the aid of intermittent galvanostatic titration (C/10) at the beginning, and after every 50 cycles, i.e. cycle # 0, 50, 100, 150, and 200.

3. RESULTS AND DISCUSSION

3.1. From Slurry to the Porous Electrode: A Simple Design Framework

Preparation of bilayer electrodes with a well-defined level of heterogeneity requires a careful adjustment of the design variables including the solid volume fraction and viscosity of the slurry, among others. These parameters are very sensitive to the slight variations in the carbon loading and turn out to be the most crucial parameters in determining the final structure and performance of the resulting electrodes. These interdependences are revealed and spotlighted in the subsections 3.1 and 3.2 with a general application for an efficient design of battery porous electrodes. Here, by formulation we refer to the state of electrode slurry which is well defined by the chemical identity of every component i, mass fractions in the solid component (f_i) and the mass ratio between the solvent and solid (ss). Only three independent design variables are sufficient to unequivocally describe the state of a slurry which is composed of a single type of active-material ($i = 'a'$), conductive carbon ($i = 'c'$), and binder ($i = 'b'$) dispersed in a single solvent (e.g. NMP). We assume that a hypothetical binder film [39] with the thickness t_b is

uniformly distributed over the surface of active material and carbon (See SI, eqn.S1). Therefore, t_b together with one of the f_i variables (either fraction of carbon or active material) can set the solid formulation in the slurry. In our experiments, a same value of binder thickness (t_b=const.) is used in all formulations with the implication that the mechanical integrity such as adherence to the current collector and the mechanical stability of the porous structure are quite similar independent of formulation. Highlighting the importance of ss and the total solid volume fraction in the slurry ($\emptyset$), we define a new parameter, t_s, that is the thickness of a hypothetical solvent shell covering uniformly the surface of active-material and carbon particles (See SI, eqn.S2). The following useful approximation can be readily derived (See SI, eqn.S1-5) accentuating the interdependence among $\emptyset$, t_s, and f_c

$$\frac{1}{\emptyset} \approx \Theta_1(t_s, f_c) \approx 1 + \frac{\rho_a(S_a + S_c f_c)}{1 - f_c} t_s \quad (1)$$

Therefore, the state of each slurry formulation can be determined by the set of t_b, f_c , and t_s parameters (refer to Table S1). The solid volume fraction in the slurry ($\emptyset$) has a significant influence on the viscosity (η) of the electrode slurry [41] (eqn.S6), and according to eqn.1, $\emptyset$ is less sensitive to the f_c than it is to the t_s, i.e. $\left.\frac{\partial \emptyset}{\partial f_c}\right|_{t_s} < \left.\frac{\partial \emptyset}{\partial t_s}\right|_{f_c}$. This means that for small variations in f_c, the slurry viscosity (η) can be approximated as a single-variable function of t_s:

$$\eta \approx \Theta_2(t_s) \quad (2)$$

A series of slurry formulations was prepared by varying the fraction of carbon (f_c) and thickness of solvent shell (t_s) while keeping the thickness of binder film constant at $t_b = 13$ nm. We set up two different groups of formulations. The first group consists of 9 formulations equally distributed according to their t_s values ($0.36, 0.64, 1.35$ μm) in 3 subsets. In the second group, 3 subsets are formed by the formulation groups differing in their $\emptyset$ values ($0.17, 0.2, 0.24$). Hereafter, we refer to the first and second groups by iso-t_s and iso-$\emptyset$ formulations, respectively.

The viscosity of the iso-t_s samples were measured at shear rates between 1-500 1/s and the results are summarized in Fig. 1a and b. The viscosity vs. shear rate plots of the slurries with the same solvent thickness almost coincide on each other (Fig. 1a) irrespective of the carbon content. It is noteworthy that $\emptyset$ increases by decreasing f_c at

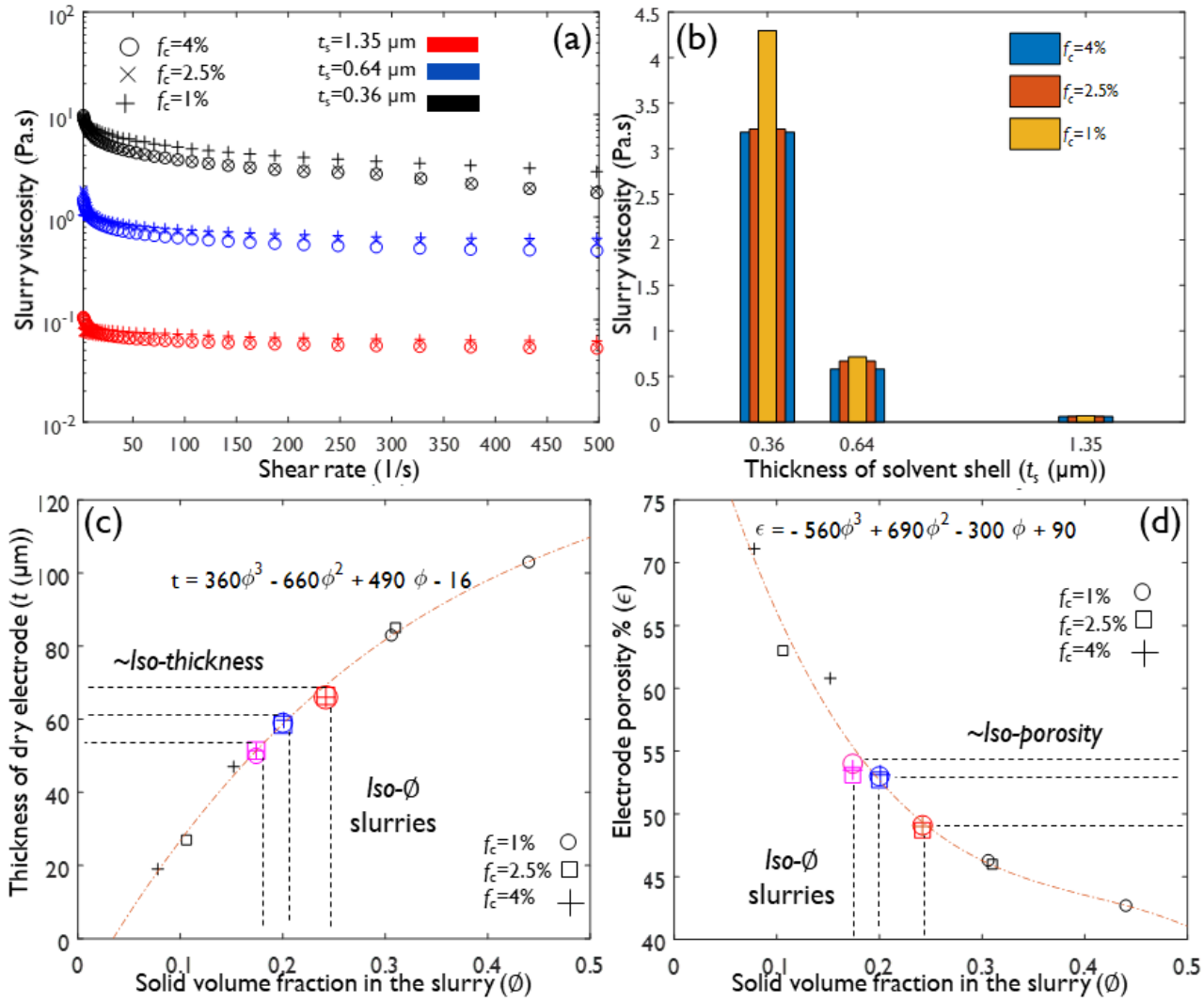

Figure. 1. a) Viscosity vs. shear rate for the slurries made of three carbon fractions f_c of 1%, 2.5%, and 4% at three different thickness for solvent shell t_s of 0.36 (black), 0.64 (blue), and 1.35 (red) µm, b) the corresponding correlation between the viscosity (at shear rate of 142 1/s) and t_s for slurries with f_c of 1%, 2.5%, and 4%. c) Dry thickness and d) non-calendered porosity as a function of solid-volume fraction (Ø). The pink, blue, and red markers represent the three iso-Ø formulations and the black markers belong to the three iso-t_s formulations. The circle, square, and plus markers identify the formulations with 1, 2.5, and 4% of carbon, respectively. All the electrodes were fabricated at a doctor blade gap of 235 µm.

constant t_s, and thus eqn.2 becomes less accurate at lower f_c in the wake of increased significance of particle-particle interactions in a concentrated slurry. [42]

In order to prepare bilayer electrodes, we used slurries sharing the same values of t_s and t_b while differing in f_c. The formulation 94:2.5:3.5 (f_a^0:f_c^0:f_b^0) was used as a reference in the preparation of NMC electrodes, that

corresponds to t_b =13 nm, and t_s =0.64 μm (Table S1). The bilayer electrodes (Table 1) consisted of six groups denoted by (f_c^1, f_c^2) where the total carbon loading of 2.5 wt.% was distributed between a layer close to the current collector ($f_c^1 = x$) and a layer on top ($f_c^2 = y$). We ascribe a heterogeneity factor 0<δ<1 to each bilayer electrode defined by the mass-averaged relative deviation in the carbon fraction from the mean value (f_c^t):

$$\delta = \sum_i \frac{\omega^i}{\omega^t} \left| \frac{f_c^i - f_c^t}{f_c^t} \right| \quad (3)$$

where ω^i and ω^t stand for the solid loading in layer 'i' and total solid loading in the bilayer, respectively.

3.2. Microscopic Heterogeneity

To better understand the impact of heterogeneity on the cell performance, it is useful to highlight the important links between the non-uniformity in the carbon distribution and the spatial variance in the electrode's porosity and thickness. According to Fig.1c-d it is intuitive to conclude that the thickness (t) and porosity (ϵ) of the dry electrodes significantly correlate with the solid volume fraction in the slurry ($\emptyset$):

$$t \approx \Theta_3(\emptyset) \quad (4)$$

$$\varepsilon \approx \Theta_4(\emptyset) \quad (5)$$

Three data clusters, that are related to the iso-$\emptyset$ slurries, are observed in the range $0.15 < \emptyset < 0.25$ each composed of 3 formulations with almost identical coordinates (pink, blue and red markers in Fig. 1c-d). The remaining data points (black markers) that are falling outside the $0.15 < \emptyset < 0.25$ range belong to the sets of iso-t_s formulations that were discussed earlier. All electrodes were prepared with the same blade gap. The dry thickness and porosity values are similar for iso-$\emptyset$ electrodes regardless of their carbon content or t_s, i.e. viscosity.

Table 1. The formulation of 6 groups of bilayer NMC porous electrodes with a non-uniform distribution of carbon between the two layers.

Total carbon loading (f_c^t)	(f_c^1, f_c^2) (x, y)	heterogeneity factor (δ)	fraction of the total mass of active material (ω_a^t) residing in each layer (ω_a^i)	
			$\frac{\omega_a^1}{\omega_a^t}$	$\frac{\omega_a^2}{\omega_a^t}$
0.025	(0.02, 0.03)	0.2	0.505	0.495
0.025	(0.015, 0.035)	0.4	0.511	0.489
0.025	(0.01, 0.04)	0.6	0.516	0.484
0.025	(0.03, 0.02)	0.2	0.495	0.505
0.025	(0.035, 0.015)	0.4	0.489	0.511
0.025	(0.04, 0.01)	0.6	0.484	0.516

A simple physical picture can be hypothesized to draw a direct link between the non-uniformity of a slurry and the microstructural heterogeneity in the resulting electrode. Fig 2a and 2b schematize the uniform and non-uniform, respectively, distribution of the active-material (green circle) and carbon additive (grey circle) particles among the three neighboring α, β, γ portions of a hypothetical electrode slurry at rest. In the both configurations, the three regions happen to share the same thickness of the solvent shell which has been roughly visualized by the same inter-particle distance in the $\alpha, \beta,$ and γ regions. Under such circumstances, and following eqn.2, the local viscosity values for $\alpha, \beta,$ and γ are the same. Although an iso-t_s state in the slurry is in favor of a quasi-equilibrium between the neighboring regions but it does not necessarily secure an iso-$\emptyset$ state. Therefore, it is legitimate to visualize a quasi-equilibrated configuration in which the slurry is segmented to the iso-t_s zones but with a non-uniform fractional occupation of the volume by the solid phase ($\emptyset$). The non-uniformity of $\emptyset$ might be induced by an uneven distribution of the carbon (Fig 2b) among iso-t_s zones according to eqn.1. Such a non-uniform distribution of carbon in the slurry, notwithstanding the possible further impact of the non-ideal drying conditions, will result in a dry electrode with an intrinsic non-uniform porosity, i.e non-uniform tortuosity [11] and/or thickness on account of eqns 4-5. The roughness analysis of the electrodes' surface supports this hypothesis where a direct correlation between f_c and the height distribution is observed (Fig S2) which is the effect of solvent and the increase in the ratio of nanometric to micrometric mass in the porous electrode. [43] A qualitative demonstration of the as described phenomena has been exemplified in Fig.2c-d putting the SEM cross-sections of two NMC electrodes with visible contrast in the heterogeneity level with regards to the distribution of the porosity and solid content. We speculate that a non-uniform slurry as such is an important origin for the in-plane utilization inhomogeneity of active materials, [20,44–47] or the poor performance of electrodes formulated with a dilute slurry. [25] A closer look at Fig. 1c-d reveals that porosity and thickness are more sensitive to and stronger functions of the solid volume fraction for slurries with $\emptyset < 0.2$. This observation suggests that slurries made with high solvent or carbon content are more prone to the spatial variations of porosity given the macroscale thickness and porosity are influenced by the interplay between the solid and liquid components of the slurry at the microscale. Hereafter, this work focuses on the impact of carbon non-uniformity on the electrochemical performance of NMC porous electrodes.

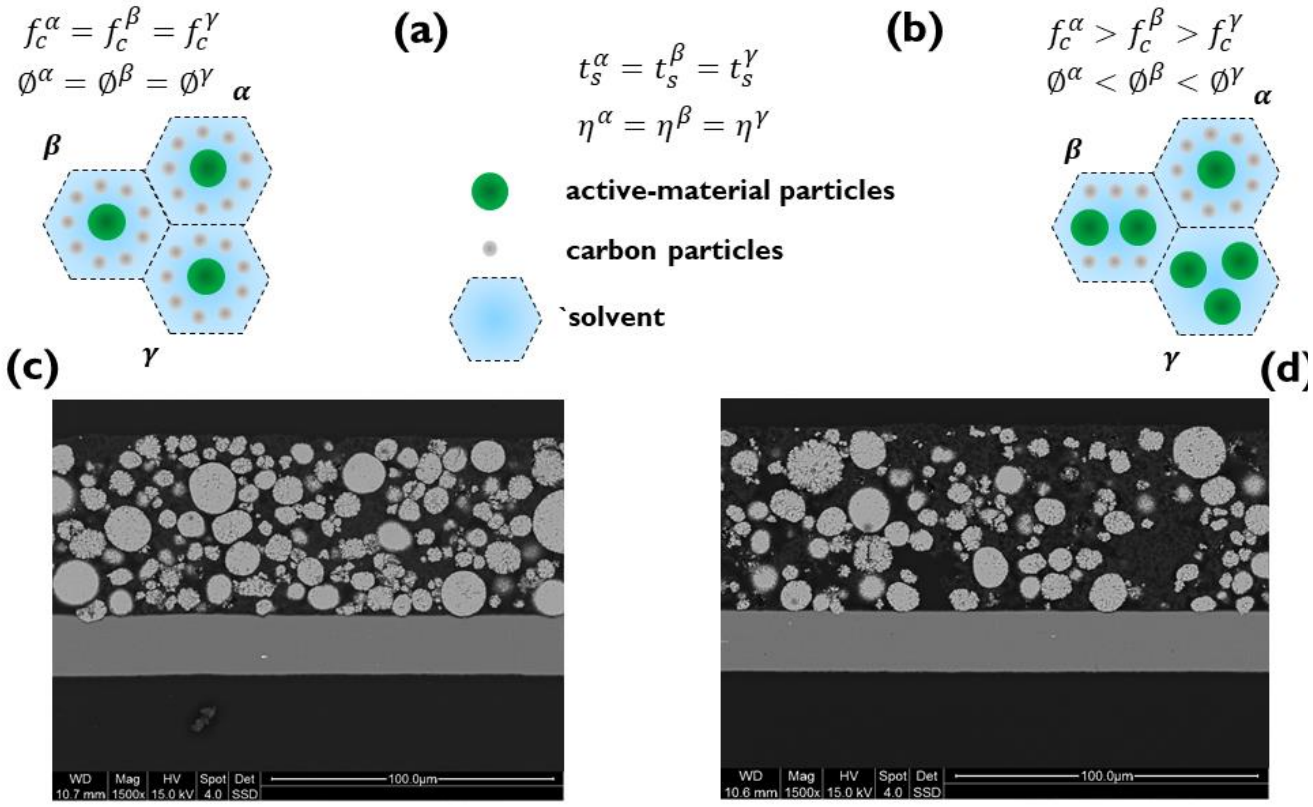

Figure 2. Hypothetical electrode slurries with (a) uniform (b) non-uniform distribution of the active-material and carbon particles between the three neighboring regions with equal thickness of the solvent shell and viscosity. The cross sectional images of the NMC porous electrodes with (c) homogeneous and (d) heterogeneous distribution of carbon and NMC particles corresponding to the hypothetical slurries in Fig.2a and Fig.2b, respectively. The SEM cross sections were taken from a single layer NMC electrode prepared from the same batch with the formulation: (f_c=4%,$\emptyset = 0.152$).

This is realized by using the bilayer electrodes formulated with a controlled through-plane heterogeneity of carbon distribution between the two layers (Fig. 3a-b).

3.3. Bilayer Electrodes: a model system to quantity the impact of heterogeneity on the electrode performance

3.3.1. Heterogeneity and Rate Performance

We used an empirical formalism in analogy with the Peukert's law [48,49] to quantify the sensitivity of the energy or capacity (Y) to the (dis)charge current in single layer and bilayer electrodes (Fig. S3)

$$Y_j = \beta I_j^{-\alpha} \quad (6)$$

where Y_j can be the (dis)charge energy or capacity at the C-rate I_j. α>0 and $\beta > 0$ are the two series of constants which are refined via a least-square fitting of the experimental data at different C-rates, i.e. I_j=1/2, 1, 2, 3 (Fig. S4). The capacity during galvanostatic (dis)charge, in a given voltage window, tends downward when the current increases due to the ensemble of kinetics and transport limitations in the electrode and electrolyte phases. Such a tendency can be quantified for an electrode design or formulation by the α exponent in eqn.6 as a lumped indicator: for every doubling in the current, the energy will drop by an approximate factor of $\gamma = 0.301^{\alpha}$, hereafter referred to as the rate-capability coefficient. Therefore, the electrode designs with a smaller γ value are more vulnerable to the rate limitations. Although similar sensitivity analyses can be conducted by using the capacity or energy data and for both discharge and charge experiments, here, we report the γ values based on the discharge energy. This is the most comprehensive index which is indicative of not only the capacity decrease but also the rise in the cell impedance. The γ values based on the discharge energy are presented in Fig.3c for the NMC electrodes as a function of carbon content (f_c) in the single layer electrodes and the carbon fraction in the bottom layer (f_c^1) of the bilayer electrodes.

The rate-capability coefficient drops from 0.9 to below 0.85 when f_c (f_c^1) is lowered from 4 to 1.5 wt.%. Further decrease of carbon to 1 wt.% in the electrode formulation is concurrent with a significant drop of γ to less than 0.7 (Fig.3c). The rate capability of the bilayer electrodes exhibits a very similar trend to the single layer electrodes (Fig.3c) when compared against the carbon fraction in the bottom layer.

This observation suggests that the layer close to the current collector has the dominant role in determining the rate capability of our heterogeneous bilayer electrodes. Such a hypothesis would also imply that in the bilayer porous electrodes, the long-range electronic transport is the rate limiting step relative to the ionic transport. The analysis of electronic and ionic transport phenomena (Fig. S5) confirms that unlike the electronic conductivity (Fig. S5a) the bulk tortuosity remains relatively insensitive (Fig. S5b) to the carbon content in the NMC porous electrodes. This observation is at odd with previous reports over the variation trends of tortuosity with carbon content in the porous electrodes of lithium-ion batteries. For instance, Landesfeind et al.[30,50] reported a decrease in tortuosity with increasing the carbon content for LFP cathode and graphite anode. An opposite trend was observed by Itou et al. [51] for the $LiNiCoALO_2$-based electrodes. In our bilayer electrodes, the top layer irrespective of the

formulation sets up a rather similar ionic percolation path between the separator and the bottom layer. The configuration of the electronic percolation network between the current collector and the top layer is however a strong function of the carbon content in the bottom layer. It is noteworthy that for the sake of simplicity in analysis, here, we used the same processing steps of mixing, drying, calendaring, as well as electrode thickness, and slurry

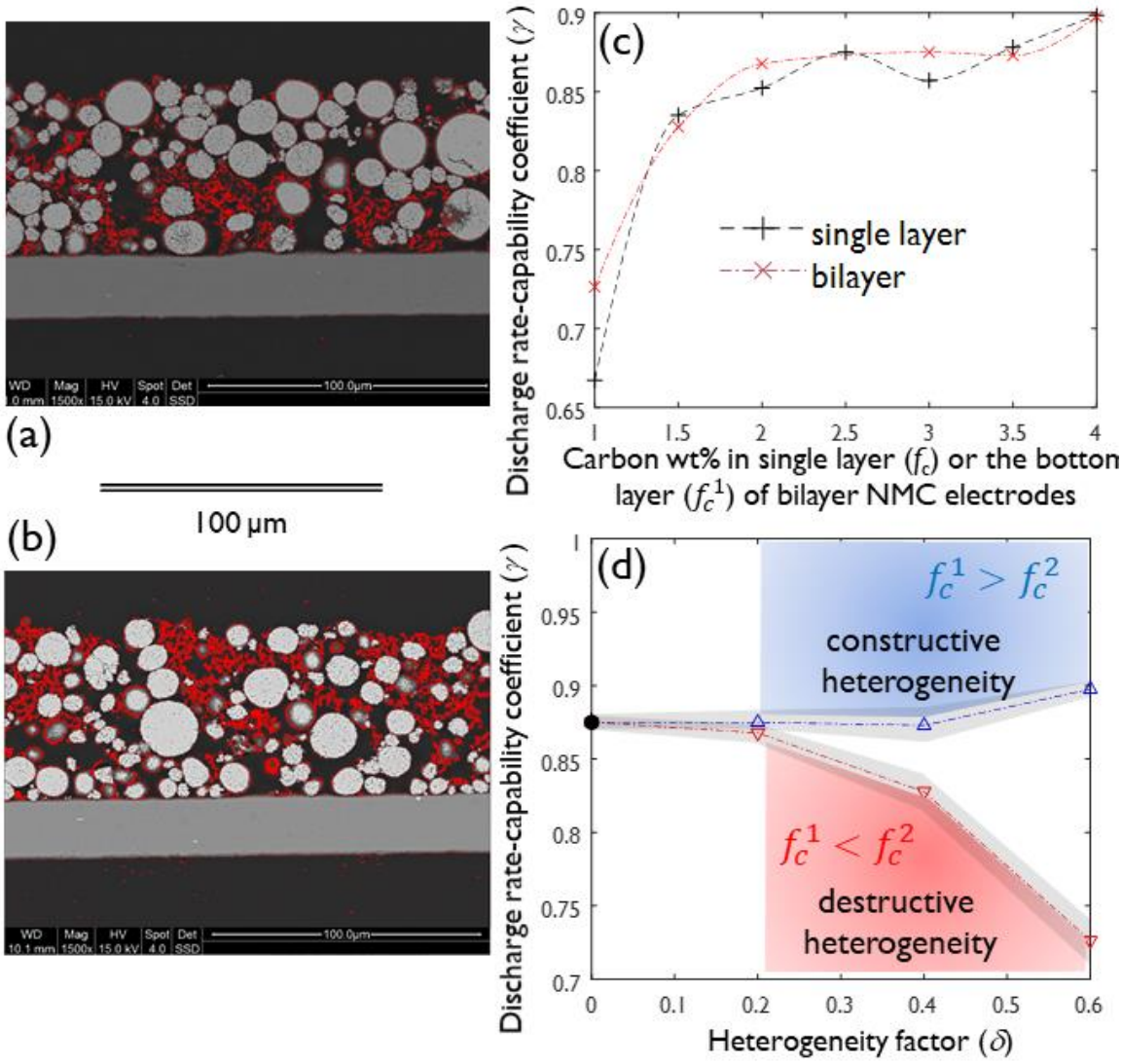

Figure. 3. Color-enhanced SEM cross-section images of the two bilayer porous electrode with (a) bottom layer of 4 wt.% C ($f_c^1 = 0.04$), and a top layer of 1 wt.% C ($f_c^2 = 0.01$), (b) bottom layer of 1 wt.% C, and a top layer of 4 wt.% C. (c) Rate-capability coefficient (γ) based on the discharge energy in the single layer (dash) and bilayer (dash-dot) NMC electrodes as a function of carbon content in the single layer and bottom layer, respectively. (d) the segregation of the bilayer electrodes in the two groups of constructive (blue zone, $f_c^1 > f_c^2$) and destructive (red zone, $f_c^1 < f_c^2$) heterogeneity on the basis of positive and negative deviation of the rate-capability coefficient from that of the single-layer design. The gray highlighted area represents the uncertainty of the results due to the experimental errors and error propagation (see SI).

viscosity to minimize the disparity between the electrodes with respect to the morphology of carbon-binder domains. [13,15,52–55] The six bilayer electrodes when juxtaposed with their single layer counterpart (black circle, Fig.3d) segregate in two categories of constructive and destructive heterogeneity.

The rate capability is superior (blue zone in Fig.3d) and inferior (red zone in Fig.3d) to the single layer design in the latter and former groups, respectively. The performance deviation of the bilayer electrodes from the single layer design is correlated to the heterogeneity factor and the position of the low-carbon layer. In the heterogeneity zone of $0 < \delta < 0.6$, the pristine NMC bilayer electrodes with a carbon-rich layer close to the current collector ($f_c^1 > f_c^2$) outperform the single layer design (Fig.3d).

It is legitimate to assume that the active-material utilization in the bottom layer would be very close to that of a single layer design with identical formulation. This assumption is made on the grounds that the electronic transport is identified to be a more limiting factor to the performance of our bilayer electrodes compared to the ionic limitations. This hypothesis implies that the ionic resistance induced by the top layer against the reaction front in the bottom layer has negligible effect in limiting the capacity of the bottom layer for the range of electrode thicknesses and C-rates investigated in this study. This assumption enables us to approximate the utilization degree of the top layer at C-rate j (Q_t^j) using eq.7 of which the accuracy awaits verification by the in-operando techniques in the future studies

$$Q_t^j = \omega_a^1 u_1 Q_1^j + \omega_a^2 u_2 Q_2^j \tag{7}$$

where ω_a^1 and ω_a^2 are the active material loading ratios in the bottom and top layers, respectively. Q_1^j and Q_2^j are the discharge capacity at C-rate j of the bottom and top layers, respectively, in their standalone design, i.e. single layer electrode. $u_1 = 1$ and u_2 are defined as the utilization coefficients for the active-material in each of the layers relative to their stand-alone designs.

The uniformity in utilization of the active material between the two layers at C-rate j can be quantified using a disparity coefficient (ψ)

$$\psi_j = \frac{Q_1^j}{u^2 Q_2^j + Q_1^j} = \frac{\omega_a^2}{\omega_a^2 - \omega_a^1 + \frac{Q_t^j}{Q_1^j}} \tag{8}$$

where $\psi_j \neq 0.5$ implies an uneven contribution from the two layers in the total capacity of the bilayer electrode. $\psi_j > 0.5$ and $\psi_j < 0.5$ highlight the higher contribution from the bottom and top layers, respectively, according to eqn.8.

The active material in all bilayer electrodes are being utilized almost uniformly (Fig.4a) except in the electrode with a heterogeneity factor of 0.6 and with the low carbon layer at the bottom. There are multiple reports on the preferential utilization and degradation of the electrodes in the areas close to the separator due to the better exposure to the lithium ions in the electrolyte. [56] Here our findings show that a non-uniform utilization could be induced as well by the disparity in the electronic percolation network. Figure 4a (red squares) suggests that in the bilayer electrode {f_c^1=0.01, f_c^2=0.04}, the active material utilization in the top layer is almost 1.4 times that of the

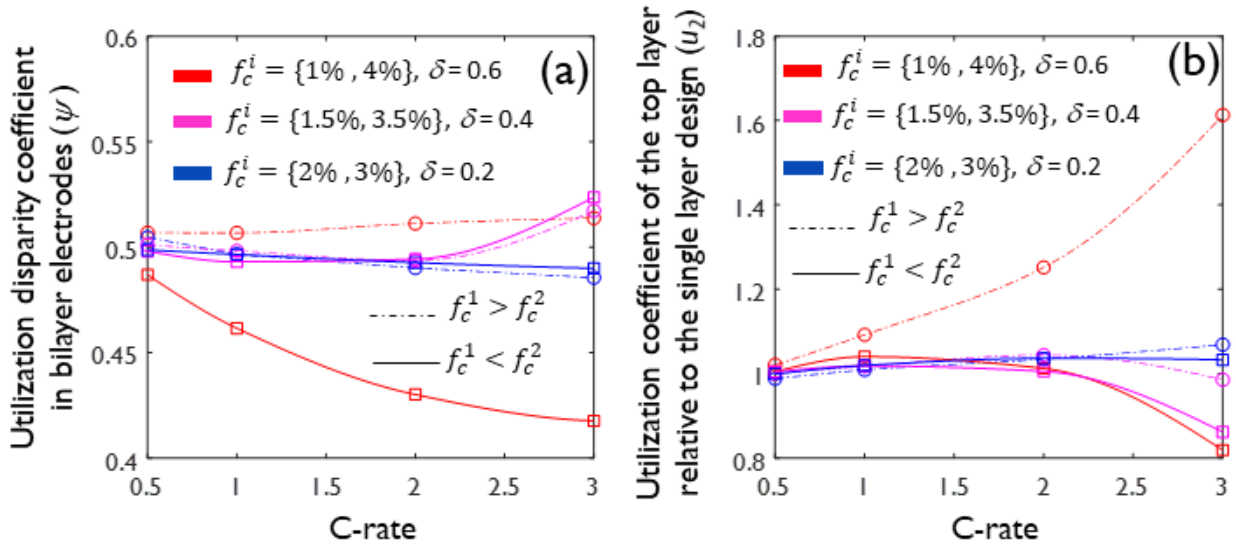

Figure. 4. a) disparity (eqn.8) in the utilization of NMC particles in the bottom versus top layer of the bilayer electrodes with different levels of heterogeneity ($\delta = 0 - 0.6$), b) degeneration or improvement in the utilization of NMC particles in the top layer of the bilayer electrodes relative to that of a single layer design (eqn.7).

bottom layer. Here, the active material particles close to the current collector are electronically less wired relative to the particles in the vicinity of the separator. This observation indirectly implies that the through-plane (z) configuration of the electronic percolation network is less limited by the presence of a bottom carbon-poor layer. There is, however, a significant disparity in the in-plane configuration (x-y) of the electronic network between the two layers.

The u_2 coefficient indicates the synergistic impact of the bottom layer on the performance of the top layer, i.e. $u_2>1$ and $u_2<1$ reflect the promotion and demotion, respectively, of the performance for the top layer compared to the single layer design. In the heterogeneous electrode with $\delta = 0.6$ and the carbon-poor layer at the bottom, u_2 drops below 1 (Fig.4b, red solid line) showing that the bottom layer is degenerating the performance of the carbon-rich layer at top due to an increased electronic transport limitation through-plane of the electrode. The opposite holds true when the position of the carbon-poor and –rich layers are swapped (Fig.4b, red dash-dot line).

3.3.2. Bilayer Electrodes: Heterogeneity and Ageing

The impact of heterogeneity on the aging behavior of NMC electrodes was investigated using longer term cycling tests at room temperature in two series of coin cells using lithium foil and $Li_4Ti_5O_{12}$ (LTO) as anode. In Li|NMC configuration, the possible loss of NMC particles can be easier identified from aging trends thanks to the unlimited reserve of lithium at the anode. The detection of irreversible loss of lithium into the side reaction products such as SEI or CEI is facilitated in the LTO|NMC cells on account of the finite source of lithium in the cell. The retention of discharge capacity over the course of 50 continuous cycles with C/2 and C/3 discharge and charge regimes, respectively, is compared in Fig.5a for three Li|NMC cells with cathodes at different heterogeneity levels. Notwithstanding the similar trends at the early stage of cycling, the cells start to exhibit very different aging dynamics with the highest and lowest rate of capacity loss for the cells made of cathode formulations $\{f_c^1$=0.01, f_c^2=0.04$\}$ and $\{f_c^1$=0.04, f_c^2=0.01$\}$, respectively. The complementary analysis (Fig.S6) of aging for the 6 bilayer electrodes and their single layer counterpart ($f_c = 0.025$) suggests that the rate of discharge energy loss is proportional to the heterogeneity factor for the electrodes with carbon-poor layer at the vicinity of current collector (Fig.5b). The constructive impact of heterogeneity in lowering the rate of energy loss is observed for the bilayer electrodes with carbon-rich layer close to the current collector when $\delta \geq 0.4$ (Fig.5b). The postmortem analyses of the recovered electrodes after 50 cycles indicate that the loss of NMC particles is a noteworthy consequence of aging in the Li|NMC cells. The C/10 galvanostatic titration of the recovered electrodes with fresh electrolyte and lithium anode highlights the lower loss of active material in electrodes with $\delta \geq 0.2$ and $f_c^1 > f_c^2$ (Fig.5c). These observations are in line with the electrochemical impedance spectroscopy results (Fig.S7). The Nyquist spectrum for the formulation $\{f_c^1$=0.04, f_c^2=0.01$\}$ remains almost intact (Fig.S7b) after 50 cycles which

validates the conclusion of negligible NMC loss drawn from the columbic titration analysis (Fig.5c). The impedance spectrum for formulation $\{f_c^1=0.01, f_c^2=0.04\}$ expands in both real and imaginary directions highlighting the loss of electrochemically active surface area, i.e. NMC loss, and the increased interfacial resistance (Fig.S7a).

The aging trends among three LTO|NMC cells are compared in Fig. 5d during 200 constant-current cycles at 1C. Discharge capacity in the cell with cathode formulation $\{f_c^1=0.01, f_c^2=0.04\}$ fades below 53% after 200 cycles which is significantly higher than those of single layer (84.3%) and the bilayer design with carbon-rich layer as the bottom coat (89.2%). These cells were subject to a series of intermittent titration at C/10 before the start of aging tests, and after every 50 cycles (Fig. S8) in order to follow the progressive evolution of lithium and NMC

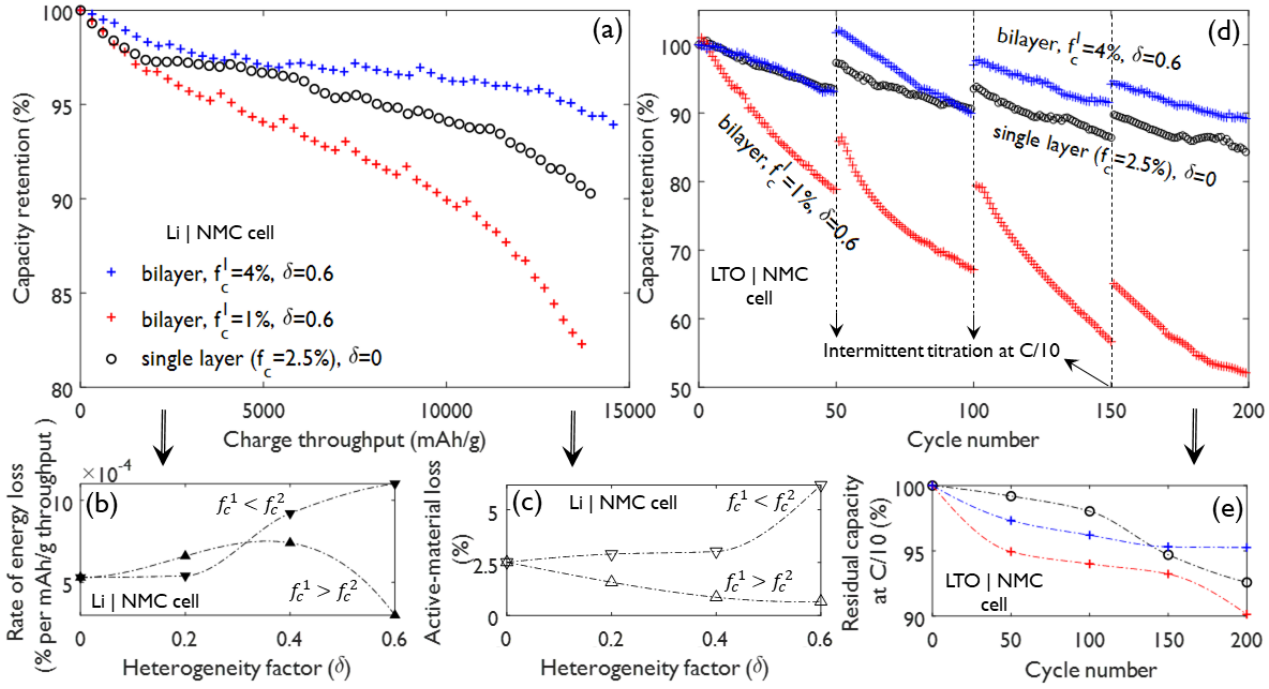

Figure. 5. a) Discharge capacity retention of Li|NMC coin cells made of NMC electrodes of different heterogeneity with bilayer (blue and red plus markers) and single layer (black circle) designs after 50 cycles at C/2, b) average rate of incremental loss (%) in discharge energy per unit of charge throughput (mAh/g) in Li|NMC cells with single and bilayer NMC electrodes, c) active material loss in Li|NMC cells after 50 cycles according to the C/10 titration of the recovered NMC electrodes with refreshed electrolyte and Li, d) discharge capacity fade in LTO|NMC cells over 200 cycles at 1C compared between single layer (black circle) and 2 bilayer NMC electrodes (blue and red plus markers), e) residual capacity of the LTO|NMC cells (subplot d) measured at the beginning and after every 50 cycles using a C/10 galvanostatic titration.

losses during cyclic aging tests. We observe a continuous decrease of residual capacity during the 200 cycles (Fig. 5e) for the single layer design (7.5%) and $\{f_c^1$=0.01, f_c^2=0.04$\}$ formulation (10%).

The smallest irreversible loss of capacity (4.8%) belongs to the formulation $\{f_c^1$=0.04, f_c^2=0.01$\}$ and seems starting to level off after 150 cycles unlike the other two cells (Fig. 5e). A closer look at the titration profiles (Fig. S8a-b) suggests the origin of irreversible loss to be a combination of both lithium and NMC loss for the single layer and $\{f_c^1$=0.01, f_c^2=0.04$\}$ designs. In contrast, the aging is dominated by the Li loss for the $\{f_c^1$=0.04, f_c^2=0.01$\}$ design evidenced by the sole shrinkage of the voltage tail along the capacity axis without any significant vertical shift of the voltage plateau (Fig. S8c). Noteworthy is the exponential correlation between the rate of capacity loss and the utilization disparity coefficient (Fig.4a) in the bilayer electrodes. Small deviations as low as 1% and 4% in the utilization disparity coefficient (at 1C) from $\psi = 0.5$ change the rate of capacity loss by 6% and 38% for $\{f_c^1$=0.04, f_c^2=0.01$\}$ and $\{f_c^1$=0.01, f_c^2=0.04$\}$ formulations, respectively, with respect to the single-layer design. The spatial variance in the state-of-lithiation for NMC particles in the electrode (uneven utilization) induces a non-uniform distribution of current and lithium pore-wall flux which will favor the buildup of weak spots at which the local effective current density and polarization go significantly beyond the average values in the electrode. Such hot spots become more vulnerable to mechanical fatigue (e.g. diffusion-induced stress) and accelerated electrolyte decomposition among other aging mechanisms. [37,57–61] Although a dedicated aging study is essential to identify the main aging mechanisms but we speculate that the loss of contact between the NMC particles and carbon-binder domains is responsible for the observed NMC loss and concurrent irreversible loss of capacity in our electrodes. [62–64]

4. CONCLUSIONS

A simple analytical framework was developed for an in-depth yet quantitative investigation of the microstructural heterogeneity in the porous electrodes of Li-ion batteries. The solvent-shell thickness and the solid volume fraction were conceptualized and highlighted as the crucial state identifiers for an electrode slurry. Combining experiment and theory, it was shown that the non-uniform distribution of carbon and active-material particles is a possible configuration for a macroscopically homogenous slurry and leads to the dry electrodes with an uneven distribution of porosity and thickness. The bilayer NMC porous electrodes with a controlled contrast of carbon fraction

between the two layers were introduced as an experimental model system to formalize the concept of heterogeneity and exploring its impacts on the battery performance and lifetime. The minute formulation gradient as small as 3% in a porous electrode of typical thickness was here showcased to have significant impact on the short- and long-term performance of Li|NMC and LTO|$LiNi_{0.6}Mn_{0.2}Co_{0.2}O_2$ cells. An irreversible capacity loss of 0.038% per cycle was recorded after 200 cycles at 1C for the LTO|NMC cell made of a single layer cathode formulated with a carbon loading of 2.5%. The aging rate was accelerated to 0.05% and decelerated to 0.024% per cycle for the analogous cells cycled using the same total amount of carbon and NMC loading but with the bilayer cathodes having 3% difference in the carbon fraction between the top and bottom layers (f_c={1%, 4%}). The non-uniform distribution of carbon between the two layers proved to be destructive and constructive when the layer close to the current collector was poor and rich in the carbon content, respectively. The constructive and destructive impacts of heterogeneity on the rate capability of the NMC electrodes were spotlighted by analyzing the rate-capability coefficient defined as the fractional decay in the discharge energy of Li|NMC cells for every doubling in the discharge current. The destructive impact was very striking manifesting in a 20% decline in the rate-capability coefficient of the bilayer NMC electrode with a carbon-poor layer in vicinity of the current collector relative to a single layer design. The bilayer electrodes introduced in this work can be easily adapted for the investigation of electrodes with other possible sources of heterogeneity such as active material chemistry, particle size, binder, and conductive agent. Although the common belief is usually to link the heterogeneity with the destructive impacts on the battery performance, our results highlight the potential constructive role of heterogeneity in designing high power and long lasting electrodes. Please be advised that the slurry composition and the details of the processing conditions can significantly impact the microstructural details of the resulting porous electrodes.[49] As such, care should be taken before generalizing the findings reported here to other electrode systems. For instance, the physical and chemical characteristics of the carbon conductive additive, [65,66] binder, [39,67] solvent, [68] and the loading of active-material, [69] among others, are noteworthy parameters that can limit the relevance of the conclusions drawn from the present study to other systems.

SUPPORTING INFORMATION

Analytical framework for the electrode formulation, bilayer fabrication method, tortuosity and electronic conductivity measurements, surface SEM and roughness analyses, and complementary details of electrochemical measurements.

ACKNOWLEDGMENTS

The authors are grateful for financial support to FWO-Vlaanderen (SBO XL-Lion, S005017N) and the Special Research Fund BOF of Hasselt University. S. Y. and M.S. acknowledge the fruitful discussions with Prof. Naveen Reddy.

REFERENCES

(1) Manthiram, A. An Outlook on Lithium Ion Battery Technology. *ACS Cent. Sci.* **2017**, *3*, 1063–1069.

(2) Larcher, D.; Tarascon, J.-M. Towards Greener and More Sustainable Batteries for Electrical Energy Storage. *Nat. Chem.* **2015**, *7*, 19–29.

(3) Xia, Y.; Zheng, J.; Wang, C.; Gu, M. Designing Principle for Ni-Rich Cathode Materials with High Energy Density for Practical Applications. *Nano Energy* **2018**, *49*, 434–452.

(4) Aricò, A. S.; Bruce, P.; Scrosati, B.; Tarascon, J.-M.; Schalkwijk, W. van. Nanostructured Materials for Advanced Energy Conversion and Storage Devices. *Nat. Mater.* **2005**, *4*, 366–377.

(5) Xu, J.; Lin, F.; Doeff, M. M.; Tong, W. A Review of Ni-Based Layered Oxides for Rechargeable Li-Ion Batteries. *J. Mater. Chem. A* **2017**, *5*, 874–901.

(6) Zolin, L.; Chandesris, M.; Porcher, W.; Lestriez, B. An Innovative Process for Ultra-Thick Electrodes Elaboration : Toward Low-Cost and High-Energy Batteries. *Energy Technol.* **2019**, *7*, 1900025.

(7) Habedank, J. B.; Kraft, L.; Rheinfeld, A.; Krezdorn, C.; Jossen, A.; Zaeh, M. F. Increasing the Discharge Rate Capability of Lithium-Ion Cells with Laser-Structured Graphite Anodes: Modeling and Simulation. *J. Electrochem. Soc.* **2018**, *165*, A1563–A1573.

(8) Wood, D. L.; Wood, M.; Li, J.; Du, Z.; Ruther, R. E.; Hays, K. A.; Muralidharan, N.; Geng, L.; Mao, C.; Belharouak, I. Perspectives on the Relationship between Materials Chemistry and Roll-to-Roll Electrode Manufacturing for High-Energy Lithium-Ion Batteries. *Energy Storage Mater.* **2020**, *29*, 254–265.

(9) Morelly, S. L.; Gelb, J.; Iacoviello, F.; Shearing, P. R.; Harris, S. J.; Alvarez, N. J.; Tang, M. H. Three-Dimensional Visualization of Conductive Domains in Battery Electrodes with Contrast-Enhancing Nanoparticles. *ACS Appl. Energy Mater.* **2018**, *1* , 4479–4484.

(10) Harris, S. J.; Lu, P. Effects of Inhomogeneities—Nanoscale to Mesoscale—on the Durability of Li-Ion Batteries. *J. Phys. Chem. C* **2013**, *117*, 6481–6492.

(11) Kehrwald, D.; Shearing, P. R.; Brandon, N. P.; Sinha, P. K.; Harris, S. J. Local Tortuosity Inhomogeneities in a Lithium Battery Composite Electrode. *J. Electrochem. Soc.* **2011**, *158*, A1393–A1399.

(12) Etiemble, A.; Besnard, N.; Bonnin, A.; Adrien, J.; Douillard, T.; Tran-Van, P.; Gautier, L.; Badot, J.-C.; Marie, E.; Lestriez, B. Multiscale Morphological Characterization of Process Induced Heterogeneities in Blended Positive Electrodes for Lithium – Ion Batteries. *J. Mater. Sci.* **2017**, *52*, 3576–3596.

(13) Daemi, S. R.; Tan, C.; Volkenandt, T.; Cooper, S. J.; Palacios-Padros, A.; Cookson, J.; Brett, D. J. L.; Shearing, P. R. Visualizing the Carbon Binder Phase of Battery Electrodes in Three Dimensions. *ACS Appl. Energy Mater.* **2018**, *1*, 3702–3710.

(14) Morasch, R.; Landesfeind, J.; Suthar, B.; Gasteiger, H. A. Detection of Binder Gradients Using Impedance Spectroscopy and Their Influence on the Tortuosity of Li-Ion Battery Graphite Electrodes. *J. Electrochem. Soc.* **2018**, *165*, A3459–A3467.

(15) Vierrath, S.; Zielke, L.; Moroni, R.; Mondon, A.; Wheeler, D. R.; Zengerle, R.; Thiele, S. Morphology of Nanoporous Carbon-Binder Domains in Li-Ion Batteries — A FIB-SEM Study. *Electrochem. commun.* **2015**, *60*, 176–179.

(16) Jeon, D. H. Wettability in Electrodes and Its Impact on the Performance of Lithium-Ion Batteries. *Energy Storage Mater.* **2019**, *18*, 139–147.

(17) Tian, R.; Alcala, N.; O'Neill, S. J. K.; Horvath, D. V.; Coelho, J.; Griffin, A. J.; Zhang, Y.; Nicolosi, V.; O'Dwyer, C.; Coleman, J. N. Quantifying the Effect of Electronic Conductivity on the Rate Performance of Nanocomposite Battery Electrodes. *ACS Appl. Energy Mater.* **2020**, *3*, 2966–2974.

(18) Cheng, C.; Drummond, R.; Duncan, S. R.; Grant, P. S. Micro-Scale Graded Electrodes for Improved Dynamic and Cycling Performance of Li-Ion Batteries. *J. Power Sources* **2019**, *413*, 59–67.

(19) Müller, S.; Eller, J.; Ebner, M.; Burns, C.; Dahn, J.; Wood, V. Quantifying Inhomogeneity of Lithium Ion

Battery Electrodes and Its Influence on Electrochemical Performance. *J. Electrochem. Soc.* **2018**, *165*, A339-A344 .

(20) Liu, J.; Kunz, M.; Chen, K.; Tamura, N.; Richardson, T. J. Visualization of Charge Distribution in a Lithium Battery Electrode. *J. Phys. Chem. Lett.* **2010**, *1*, 2120–2123.

(21) Sasaki, T.; Villevieille, C.; Takeuchi, Y.; Çetinel, F. Understanding Inhomogeneous Reactions in Li-Ion Batteries: Operando Synchrotron X-Ray Diffraction on Two-Layer Electrodes. *Adv. Sci.* **2015**, *2*, 1500083.

(22) Bauer, W.; Nötzel, D.; Wenzel, V.; Nirschl, H. Influence of Dry Mixing and Distribution of Conductive Additives in Cathodes for Lithium Ion Batteries. *J. Power Sources* **2015**, *288*, 359–367.

(23) Westphal, B. G.; Mainusch, N.; Meyer, C.; Haselrieder, W.; Indrikova, M.; Titscher, P.; Bockholt, H.; Viol, W.; Kwade, A. Influence of High Intensive Dry Mixing and Calendering on Relative Electrode Resistivity Determined via an Advanced Two Point Approach. *J. Energy Storage* **2017**, *11*, 76–85.

(24) Kraytsberg, A.; Ein-Eli, Y. Conveying Advanced Li-Ion Battery Materials into Practice The Impact of Electrode Slurry Preparation Skills. *Adv. Energy Mater.* **2016**, *6*, 1600655.

(25) Ligneel, E.; Lestriez, B.; Hudhomme, A.; Guyomard, D. Effects of the Solvent Concentration (Solid Loading) on the Processing and Properties of the Composite Electrode. *J. Electrochem. Soc.* **2007**, *154*, A235–A241.

(26) Zheng, H.; Yang, R.; Liu, G.; Song, X.; Battaglia, V. S. Cooperation between Active Material, Polymeric Binder and Conductive Carbon Additive in Lithium Ion Battery Cathode. *J. Phys. Chem. C* **2012**, *116*, 4875–4882.

(27) Ouyang, L.; Wu, Z.; Wang, J.; Qi, X.; Li, Q.; Wang, J.; Lu, S. The Effect of Solid Content on the Rheological Properties and Microstructures of a Li-Ion Battery Cathode Slurry. *RSC Adv.* **2020**, *10*, 19360–19370.

(28) Lim, S.; Ahn, K. H.; Yamamura, M. Latex Migration in Battery Slurries during Drying. *Langmuir* **2013**, *29*, 8233–8244.

(29) Müller, M.; Pfaffmann, L.; Jaiser, S.; Baunach, M.; Trouillet, V.; Scheiba, F.; Scharfer, P.; Schabel, W.; Bauer, W. Investigation of Binder Distribution in Graphite Anodes for Lithium-Ion Batteries. *J. Power Sources* **2017**, *340*, 1–5.

(30) Landesfeind, J.; Eldiven, A.; Gasteiger, H. A. Influence of the Binder on Lithium Ion Battery Electrode Tortuosity and Performance. *J. Electrochem. Soc.* **2018**, *165*, A1122–A1128.

(31) Hein, S.; Danner, T.; Westhoff, D.; Pri, B.; Scurtu, R.; Kremer, L.; Hoffmann, A.; Hilger, A.; Osenberg, M.; Manke, I.; Wohlfahrt-mehrens, M.; Schmidt, V.; Latz, A. Influence of Conductive Additives and Binder on the Impedance of Lithium-Ion Battery Electrodes : Effect of Morphology. *J. Electrochem. Soc.* **2020**, *167*, 013546.

(32) Lea, A.; Kremer, S.; Hoffmann, A.; Danner, T.; Hein, S.; Prifling, B.; Westhoff, D.; Dreer, C.; Latz, A.; Wohlfahrt-mehrens, M. Manufacturing Process for Improved Ultra-Thick Cathodes in High-Energy Li-Ion Batteries. *Energy Technol.* **2020**, *8*, 1900167.

(33) Gao, H.; Wu, Q.; Hu, Y.; Zheng, J. P.; Amine, K.; Chen, Z. Revealing the Rate-Limiting Li-Ion Diffusion Pathway in Ultrathick Electrodes for Li-Ion Batteries. *J. Phys. Chem. Lett.* **2018**, *9* (17), 5100–5104.

(34) Lee, B.-S.; Wu, Z.; Petrova, V.; Xing, X.; Lim, H.-D.; Liu, H.; Liu, P. Analysis of Rate-Limiting Factors in Thick Electrodes for Electric Vehicle Applications. *J. Electrochem. Soc.* **2018**, *165* (3), A525–A533.

(35) Tian, C.; Lin, F. Electrochemical Characteristics of Layered Transition Metal Oxide Cathode Materials for Lithium Ion Batteries: Surface, Bulk Behavior, and Thermal Properties. *Acc. Chem. Res.* **2018**, *51*, 89–96.

(36) Lin, F.; Markus, I. M.; Nordlund, D.; Weng, T.; Asta, M. D.; Xin, H. L.; Doeff, M. M. Surface Reconstruction and Chemical Evolution of Stoichiometric Layered Cathode Materials for Lithium-Ion Batteries. *Nat. Commun.* **2014**, *5*, 3529.

(37) Cabana, J.; Kwon, B. J.; Hu, L. Mechanisms of Degradation and Strategies for the Stabilization of Cathode-Electrolyte Interfaces in Li-Ion Batteries. *Acc. Chem. Res.* **2018**, *51*, 299–308.

(38) Li, T.; Yuan, X.-Z.; Zhang, L.; Song, D.; Shi, K.; Christina, B. Degradation Mechanisms and Mitigation Strategies of Nickel - Rich NMC - Based Lithium - Ion Batteries. *Electrochem. Energy Rev.* **2020**, *3* , 43–80.

(39) Lestriez, B. Functions of Polymers in Composite Electrodes of Lithium Ion Batteries. *Comptes Rendus Chim.* **2010**, *13*, 1341–1350.

(40) Thorat, I. V.; Stephenson, D. E.; Zacharias, N. A.; Zaghib, K.; Harb, J. N.; Wheeler, D. R. Quantifying Tortuosity in Porous Li-Ion Battery Materials. *J. Power Sources* **2009**, *188*, 592–600.

(41) Green, G. K. B. J. T. The Determination of the Bulk Stress in a Suspension of Spherical Particles to Order C^2. *J. Fluid Mech.* **1972**, *56*, 401–427.

(42) Rutgers, I. R. Relative Viscosity and Concentration. *Rheol. Acta* **1962**, *2*, 305–348.

(43) Etiemble, A.; Besnard, N.; Adrien, J.; Tran-Van, P.; Gautier, L.; Lestriez, B.; Maire, E. Quality Control Tool of Electrode Coating for Lithium-Ion Batteries Based on X-Ray Radiography. *J. Power Sources* **2015**, *298*, 285–291.

(44) Katayama, M.; Sumiwaka, K.; Miyahara, R.; Yamashige, H.; Arai, H.; Uchimoto, Y.; Ohta, T.; Inada, Y.; Ogumi, Z. X-Ray Absorption Fine Structure Imaging of Inhomogeneous Electrode Reaction in $LiFePO_4$ Lithium-Ion Battery Cathode. *J. Power Sources* **2014**, *269*, 994–999.

(45) Thomas-Alyea, K. E.; Jung, C.; Smith, R. B.; Bazant, M. Z. In Situ Observation and Mathematical Modeling of Lithium Distribution within Graphite. *J. Electrochem. Soc.* **2017**, *164*, E3063–E3072.

(46) Yu, X.; Feng, Z.; Ren, Y.; Henn, D.; Wu, Z.; An, K.; Wu, B.; Fau, C.; Li, C.; Harris, S. J. Simultaneous Operando Measurements of the Local Temperature, State of Charge, and Strain inside a Commercial Lithium-Ion Battery Pouch Cell. *J. Electrochem. Soc.* **2018**, *165*, A1578–A1585.

(47) Cai, L.; An, K.; Feng, Z.; Liang, C.; Harris, S. J. In-Situ Observation of Inhomogeneous Degradation in Large Format Li-Ion Cells by Neutron Diffraction. *J. Power Sources* **2013**, *236*, 163–168.

(48) Doerffel, D.; Sharkh, S. A. A Critical Review of Using the Peukert Equation for Determining the Remaining Capacity of Lead-Acid and Lithium-Ion Batteries. *J. Power Sources* **2006**, *155*, 395–400.

(49) Hamed, H.; Yari, S.; D'Haen, J.; Renner, F. U.; Reddy, N.; Hardy, A.; Safari, M. Demystifying Charge Transport Limitations in the Porous Electrodes of Lithium-Ion Batteries. *Adv. Energy Mater.* **2020**, *2002492*.

(50) Landesfeind, J.; Hattendorff, J.; Ehrl, A.; Wall, W. A.; Gasteiger, H. A. Tortuosity Determination of Battery Electrodes and Separators by Impedance Spectroscopy. *J. Electrochem. Soc.* **2016**, *163*, A1373–A1387.

(51) Itou, Y.; Ogihara, N.; Kawauchi, S. Role of Conductive Carbon in Porous Li-Ion Battery Electrodes Revealed by Electrochemical Impedance Spectroscopy Using a Symmetric Cell. *J. Phys. Chem. C* **2020**, *124*, 5559–5564.

(52) Ferraro, M. E.; Trembacki, B. L.; Brunini, V. E.; Noble, D. R.; Roberts, S. A. Electrode Mesoscale as a

Collection of Particles: Coupled Electrochemical and Mechanical Analysis of NMC Cathodes. *J. Electrochem. Soc.* **2020**, *167*, 013543.

(53) Trembacki, B. L.; Mistry, A. N.; Noble, D. R.; Ferraro, M. E.; Mukherjee, P. P.; Roberts, S. A. Mesoscale Analysis of Conductive Binder Domain Morphology in Lithium-Ion Battery Electrodes. *J. Electrochem. Soc.* **2018**, *165*, E725–E736.

(54) Morelly, S. L.; Alvarez, N. J.; Tang, M. H. Short-Range Contacts Govern the Performance of Industry-Relevant Battery Cathodes. *J. Power Sources* **2018**, *387*, 49–56.

(55) Zielke, L.; Hutzenlaub, T.; Wheeler, D. R.; Chao, C. W.; Manke, I.; Hilger, A.; Paust, N.; Zengerle, R.; Thiele, S. Three-Phase Multiscale Modeling of a $LiCoO_2$ Cathode: Combining the Advantages of FIB-SEM Imaging and X-Ray Tomography. *Adv. Energy Mater.* **2015**, *5*, 1401612.

(56) Yang, Y.; Xu, R.; Zhang, K.; Lee, S.; Mu, L.; Liu, P.; Waters, C. K.; Spence, S.; Xu, Z.; Wei, C.; Kautz, D. J.; Yuan, Q.; Dong, Y.; Yu, Y.; Xiao, X.; Lee, H.; Pianetta, P.; Cloetens, P.; Lee, J. Quantification of Heterogeneous Degradation in Li-Ion Batteries. *Adv. Energy Mater.* **2019**, *9*, 1900674.

(57) Li, W.; Dolocan, A.; Oh, P.; Celio, H.; Park, S.; Cho, J.; Manthiram, A. Dynamic Behaviour of Interphases and Its Implication on High-Energy-Density Cathode Materials in Lithium-Ion Batteries. *Nat. Commun.* **2017**, *8*, 14589.

(58) Gilbert, J. A.; Bareño, J.; Spila, T.; Trask, S. E.; Miller, D. J.; Polzin, B. J.; Jansen, A. N.; Abraham, D. P. Cycling Behavior of NCM523/Graphite Lithium-Ion Cells in the 3–4.4 V Range: Diagnostic Studies of Full Cells and Harvested Electrodes. *J. Electrochem. Soc.* **2017**, *164*, A6054–A6065.

(59) Wang, Q.; Shen, C. H.; Shen, S. Y.; Xu, Y. F.; Shi, C. G.; Huang, L.; Li, J. T.; Sun, S. G. Origin of Structural Evolution in Capacity Degradation for Overcharged NMC622 via Operando Coupled Investigation. *ACS Appl. Mater. Interfaces* **2017**, *9*, 24731–24742.

(60) Forouzan, M. M.; Mazzeo, B. A.; Wheeler, D. R. Modeling the Effects of Electrode Microstructural Heterogeneities on Li-Ion Battery Performance and Lifetime. *J. Electrochem. Soc.* **2018**, *165*, A2127–A2144.

(61) Qian, G.; Zhang, Y.; Li, L.; Zhang, R.; Xu, J.; Cheng, Z.; Xie, S.; Wang, H.; Rao, Q.; He, Y.; Shen, Y.; Chen, L.; Tang, M.; Ma, Z. F. Single-Crystal Nickel-Rich Layered-Oxide Battery Cathode Materials:

Synthesis, Electrochemistry, and Intra-Granular Fracture. *Energy Storage Mater.* **2020**, *27* , 140–149.

(62) Liu, H.; Foster, J. M.; Gully, A.; Krachkovskiy, S.; Jiang, M.; Wu, Y.; Yang, X.; Protas, B.; Goward, G. R.; Botton, G. A. Three-Dimensional Investigation of Cycling-Induced Microstructural Changes in Lithium-Ion Battery Cathodes Using Focused Ion Beam / Scanning Electron Microscopy. *J. Power Sources* **2016**, *306*, 300–308.

(63) Grillet, A. M.; Humplik, T.; Stirrup, E. K.; Roberts, S. A.; Barringer, D. A.; Snyder, C. M.; Janvrin, M. R.; Apblett, C. A. Conductivity Degradation of Polyvinylidene Fluoride Composite Binder during Cycling: Measurements and Simulations for Lithium-Ion Batteries. *J. Electrochem. Soc.* **2016**, *163*, A1859-A1871.

(64) Jiang, Z.; Li, J.; Yang, Y.; Mu, L.; Wei, C.; Yu, X.; Pianetta, P.; Zhao, K.; Cloetens, P.; Lin, F.; Liu, Y. Machine-Learning-Revealed Statistics of the Particle-Carbon/Binder Detachment in Lithium-Ion Battery Cathodes. *Nat. Commun.* **2020**, *11*, 2310.

(65) Yao, F.; Pham, D. T.; Lee, Y. H. Carbon-Based Materials for Lithium-Ion Batteries, Electrochemical Capacitors, and Their Hybrid Devices. *ChemSusChem* **2015**, *8*, 2284–2311.

(66) Landi, B. J.; Ganter, M. J.; Cress, C. D.; DiLeo, R. A.; Raffaelle, R. P. Carbon Nanotubes for Lithium Ion Batteries. *Energy Environ. Sci.* **2009**, *2*, 638–654.

(67) Zhang, Z.; Zeng, T.; Lai, Y.; Jia, M.; Li, J. A Comparative Study of Different Binders and Their Effects on Electrochemical Properties of $LiMn_2O_4$ Cathode in Lithium Ion Batteries. *J. Power Sources* **2014**, *247*, 1–8.

(68) Wood, D. L.; Quass, J. D.; Li, J.; Ahmed, S.; Ventola, D.; Daniel, C. Technical and Economic Analysis of Solvent-Based Lithium-Ion Electrode Drying with Water and NMP. *Dry. Technol.* **2018**, *36* , 234–244.

(69) Zhang, X.; Verhallen, T. W.; Labohm, F.; Wagemaker, M. Direct Observation of Li-Ion Transport in Electrodes under Nonequilibrium Conditions Using Neutron Depth Profiling. *Adv. Energy Mater.* **2015**, *5*, 1–8.

Table of content Graphic